EAI Endorsed Transactions
on Scalable Information Systems
Research Article EAI.EU

Research on Intelligent Prediction Method for Dynamic Changes of Manufacturing Industrial Land Based on Graph Attention and Spatial Decoding

Yuxuan Hu[1], Yinan Lin[1*]

[1]East China University of Science and Technology, Shanghai, China

Abstract

Recent advances in artificial intelligence have enabled effective modeling of complex industrial spatial systems. Predicting dynamic changes in manufacturing industrial land remains challenging due to spatial heterogeneity and temporal evolution across multiple influencing factors. This study develops a computational framework that integrates graph attention networks and Transformer-based temporal modeling with a spatial decoding module to forecast manufacturing industrial land change. Historical multi-source data spanning 2014 to 2023 are structured as a spatiotemporal graph, with nodes representing spatial units and edges encoding spatial proximity, transportation connections, and functional similarity. Graph attention networks learn the influence of neighboring units, while the Transformer captures temporal dependencies across consecutive periods. The spatial decoding module converts node-level predictions into geographic maps, generating interpretable probability and classification outputs. Experiments demonstrate that the proposed method outperforms baseline models in node-level classification with an accuracy of 0.768 and a Macro-F1 score of 0.712, achieves high spatial consistency with a Kappa of 0.668 and a mean intersection over union of 0.498, and accurately predicts manufacturing industrial land change intensity with a mean absolute error of 0.077 and an R^2 of 0.765. A component-wise ablation experiment further evaluates the contributions of the main model components. The results show that combining spatial graph modeling with temporal deep learning provides a robust computational approach for manufacturing industrial land change prediction and supports data-driven industrial land planning decisions.

Keywords: Manufacturing industrial land change, Spatiotemporal prediction, Graph attention network, Transformer, Spatial decoding.

Received on 04 August 2026, accepted on 03 September 2026, published on 18 September 2026

doi: 10.4108/eetsis.14321

1. Introduction

In recent years, artificial intelligence has become an important computational paradigm in advanced manufacturing and industrial systems [1-2]. With the rapid accumulation of multi-source geographic data, transportation data, points of interest, and socioeconomic information, urban land-use change analysis is shifting from traditional rule-based deduction toward data-driven intelligent prediction. Compared with other urban land-use types, manufacturing industrial land exhibits stronger sensitivity to transportation accessibility, personnel and production activity, industrial agglomeration, and regional economic vitality, resulting in more pronounced spatial heterogeneity and temporal dynamics. Therefore, developing an AI-based framework that can jointly capture spatial dependence, temporal evolution, and multi-source feature interactions is of clear significance for dynamic manufacturing industrial land prediction and refined industrial land planning.

Existing research on land use change can be mainly summarized into two categories. One category is rule-driven or scenario-driven models represented by CA-Markov [3], CLUE-S [4] and PLUS [5]. These methods are mature in land transition probability estimation, spatial allocation and future scenario simulation, and are suitable for regional-scale land use pattern deduction. However, they usually rely heavily on prior rule setting and may not fully mine the high-dimensional nonlinear relationships among multi-source urban attributes. For manufacturing industrial land, previous studies have reported pronounced spatial variation and close associations between industrial land conversion and transport corridors or road nodes [6-7]. The other category is data-driven models represented by deep-learning land-use simulation and neural representation learning of urban functional data [8-9], which can automatically extract complex nonlinear features through sample learning. Nevertheless, raster-based models alone may inadequately encode irregular relationships among spatial units; recent multimodal land-use studies have therefore emphasized the complementary value of raster and graph-topological features [10].

Graph neural networks [11-12] provide a flexible way to model irregular urban spatial units and their relational structure. Graph Convolutional Networks (GCNs) [13-14] aggregate neighbourhood information directly on graph structures, while graph-based urban land-use studies further demonstrate the value of incorporating spatial adjacency and surrounding-unit information into node representations [15]. Graph Attention Networks (GATs) [16-17] learn differentiated weights for neighbouring nodes, which is useful when the influence of surrounding industrial units is spatially heterogeneous. The Transformer architecture [18] uses self-attention for sequence modelling and can capture dependencies across multiple historical periods. Recent land-change studies combining deep spatial feature extraction with temporal sequence modelling have also demonstrated the importance of jointly considering spatial heterogeneity and temporal dependence in urban land-use forecasting [19-20].

To address the above issues, this study proposes an intelligent prediction framework for dynamic manufacturing industrial land change by integrating graph attention, Transformer-based temporal modelling, and spatial decoding. First, a multi-relational spatiotemporal graph is constructed to jointly represent spatial adjacency, transportation connectivity, and functional similarity among spatial units. Second, a graph attention and Transformer coupled architecture is designed to model heterogeneous neighbourhood influence and long-term temporal evolution in a unified manner. Third, a spatial decoding module is introduced to project node-level predictions back to geographic space, generating interpretable probability maps and spatial distribution results. On this basis, experiments are conducted to evaluate the proposed method from the perspectives of node-level classification, spatial consistency, and continuous change intensity prediction.

2. Study Area and Data Sources

2.1. Overview of the Study Area

This paper takes the main manufacturing areas and key industrial expansion zones of a city as the research object. As a large-scale regional transportation hub and highly concentrated economic activity centre, the city has long been undergoing rapid industrialization and continuous restructuring of its spatial structure, with significant evolution of land-use patterns and a representative form of manufacturing spatial organization, as shown in Figure 1. With the upgrading of the industrial structure, improvement of the transportation system, and continuous development of large-scale industrial parks and manufacturing clusters, the spatial organization of manufacturing industrial land in the city has shown an evolutionary trend from concentrated agglomeration to multi-node expansion. On the one hand, traditional manufacturing districts still maintain a remarkable state of high-intensity agglomeration; on the other hand, peripheral industrial parks, transportation corridors, and emerging development zones have gradually become important carriers for the growth of manufacturing industrial land. Manufacturing industrial land changes are sensitive to transportation accessibility, personnel and production activity intensity, regional economic activity, and the surrounding functional environment, exhibiting strong spatial heterogeneity and temporal volatility.

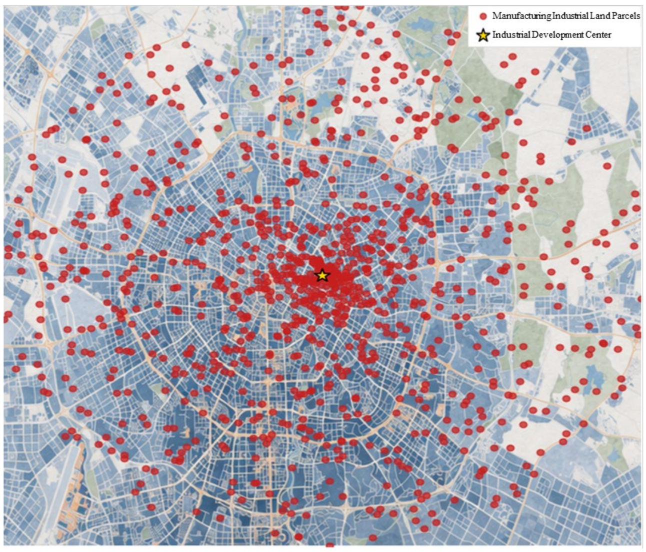

Figure 1. Spatial distribution of manufacturing industrial land parcels in the study area

2.2. Data Sources

To characterize the driving factors of manufacturing industrial land change, this study integrates multi-period spatial data from ten categories, including land use, transportation networks, industrial and supporting-facility POIs, personnel activity, regional economic activity, and industrial development. All datasets are standardized through unified projection, geometric correction, spatial matching, and temporal alignment. The temporal database retains month-level observations for dynamic variables and land change intensity, which are aggregated annually for the primary experiments while remaining available for the supplementary monthly-resolution analysis. Based on these data, multidimensional features describing industrial development, transportation accessibility, personnel and production activity, supporting environment, and location evolution are extracted for graph construction and model learning. As shown in Figure 2, the main features exhibit moderate correlations while retaining sufficient distinctiveness, supporting subsequent multi-source joint modelling.

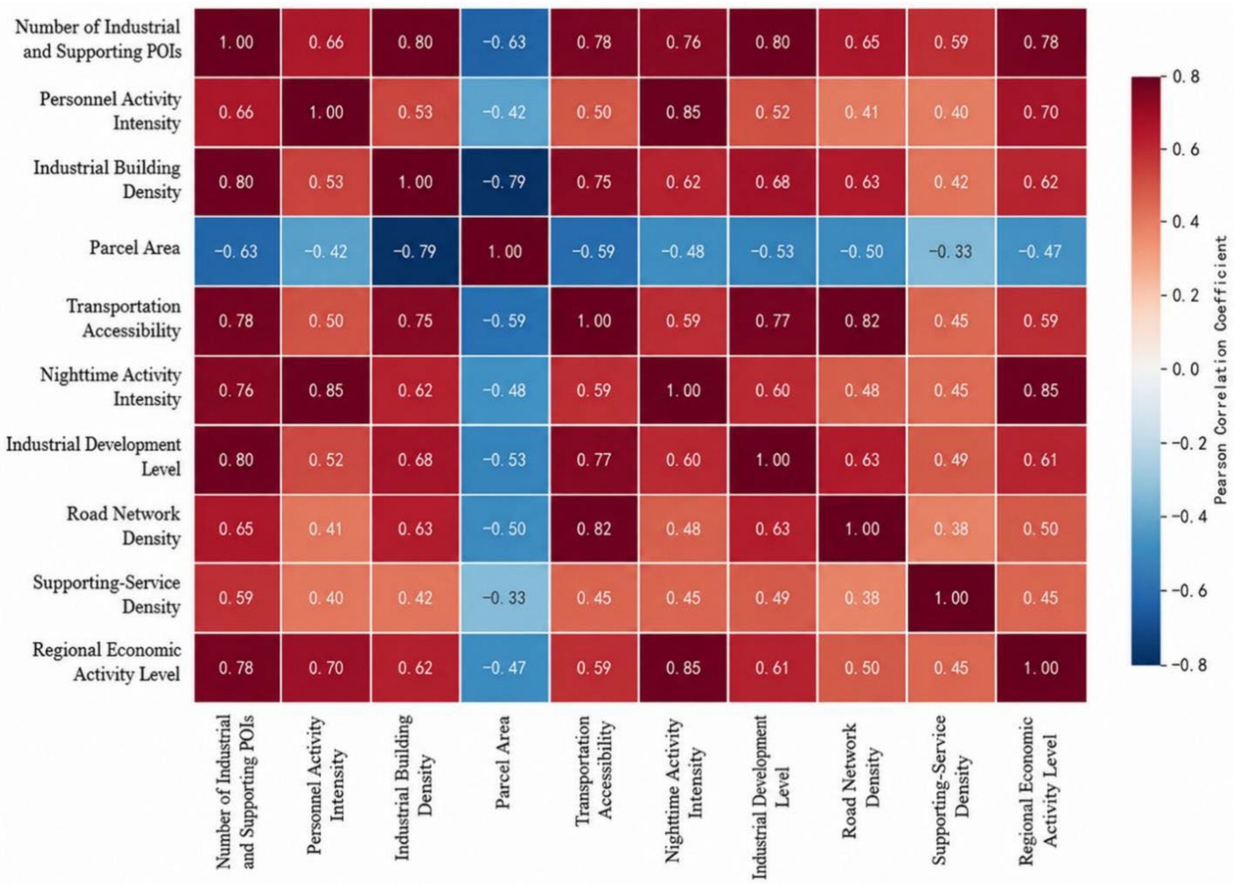

Figure 2. Correlation Heatmap of Manufacturing Industrial Land Characteristics

2.3. Feature Construction

Dynamic changes in manufacturing industrial land are not determined by a single factor but result from the combined effects of location conditions, transportation accessibility, personnel and production activity, built and supporting environment, and historical evolutionary status. To comprehensively characterize its driving mechanism, combined with manufacturing spatial development theory, laws of industrial functional organization, and data availability, this paper constructs a node feature system from five dimensions: manufacturing development foundation, transportation accessibility, personnel and production activity intensity, built and supporting environment, and location and historical evolution. Manufacturing development foundation features are mainly used to describe the existing manufacturing development level of spatial units, including the proportion of manufacturing industrial land, the proportion of surrounding manufacturing industrial land, manufacturing and supporting-facility POI density, supporting-service POI density, production-supporting POI density, and the density of business-service and administrative facility POIs. In terms of feature preprocessing, continuous features were uniformly standardized in this paper to reduce the influence of dimensional differences on model training. Categorical variables were transformed using one-hot encoding or numerical mapping; for a small number of missing values, mean imputation was adopted to ensure sample integrity and consistency of the feature matrix. All processed indicators jointly form the node input vector, which is organized into a temporal feature sequence in chronological order, serving as the basic input for the subsequent joint modelling of graph attention and Transformer.

Overall, the feature system constructed in this paper includes not only direct indicators characterizing manufacturing industrial land changes but also key driving factors such as transportation, personnel and production activity, built environment, and historical evolution. It can systematically describe the multidimensional mechanisms of dynamic changes in manufacturing industrial land and provide highly discriminative input information for subsequent spatiotemporal graph model learning.

3. Methodology

Based on the above data organization and feature construction, the methodological part of this study is further developed to model the dynamic change process of manufacturing industrial land under a unified spatiotemporal learning framework. To present the overall technical route more clearly, the complete workflow of the proposed study is illustrated in Figure 3. The framework starts from multi-source spatial data input and feature construction, and then proceeds through spatiotemporal graph representation, spatial dependency learning, temporal evolution modelling, prediction output, and spatial decoding, thereby forming an end-to-end computational pipeline for dynamic manufacturing industrial land prediction.

As shown in Figure 3, the proposed framework follows a progressive pipeline from data representation to predictive inference. Specifically, multi-period industrial spatial data are first transformed into node features and graph relations, which provide the basis for subsequent spatiotemporal learning. On this basis, the prediction task can be formalized as learning the mapping from historical node attributes and graph structures to future manufacturing industrial land change outcomes. Accordingly, the problem definition and the overall modelling framework are described in detail in the following subsection.

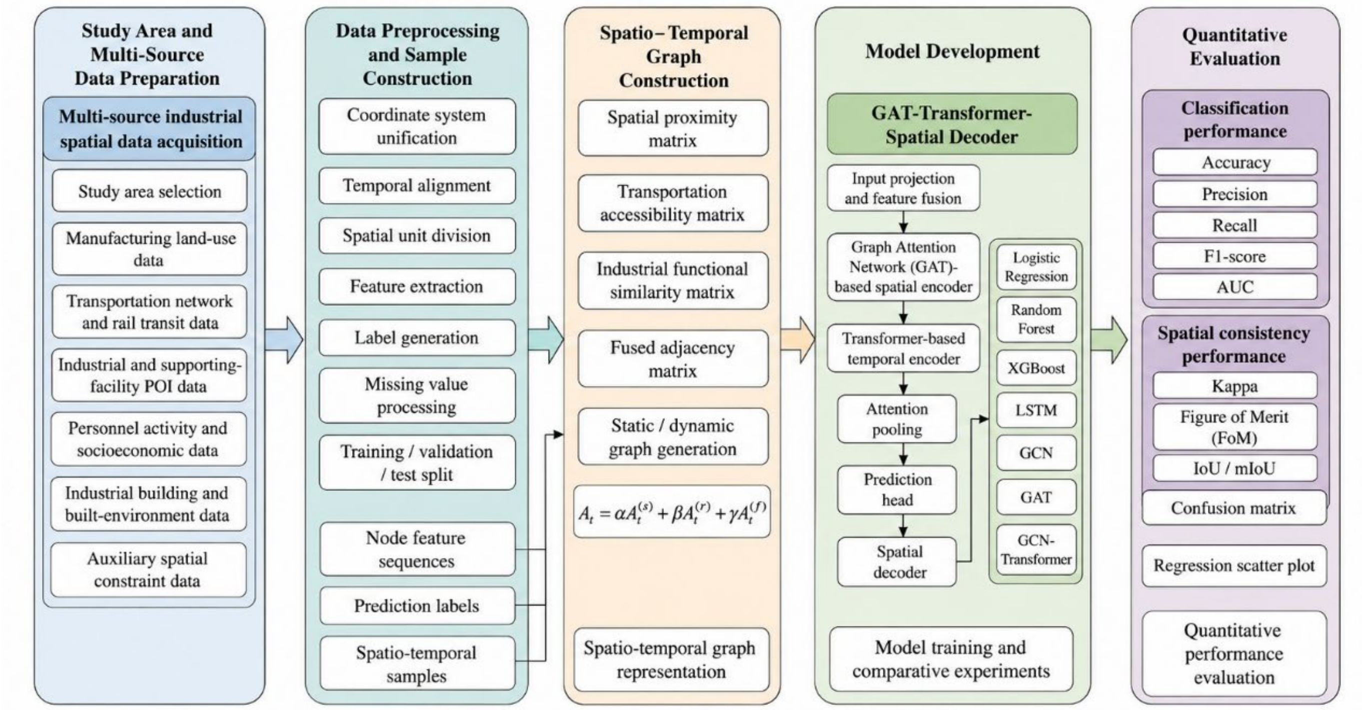

Figure 3. Research Flowchart of the proposed framework

3.1. Problem Definition and Overall Framework

The primary task of dynamic manufacturing industrial land prediction is to infer whether manufacturing land-use conversion will occur in each spatial unit at a future time from historical multi-period industrial spatial states and spatial correlation relationships. Therefore, the problem belongs to spatiotemporal joint modelling [21-22]. Let the study area be divided into N spatial units and let each spatial unit have F-dimensional attributes at time t, including manufacturing development foundation, transportation conditions, personnel and production activity, built environment, and historical change information [23]. The features of all nodes at time t are denoted as the node feature matrix:

$$X_t \in \mathbb{R}^{N \times F} \tag{1}$$

Specifically, the $i-th$ row of matrix X_t corresponds to the attribute vector of the $i-th$ spatial unit at time t. To characterize the temporal dependence of manufacturing industrial land use changes, this paper does not perform prediction using single-time-step data; instead, an input sequence consisting of T consecutive time slices is introduced, expressed as:

$$\mathcal{X} = \{X_{t-T+1}, X_{t-T+2}, \dots, X_t\} \quad (2)$$

where X denotes the historical observation window of the model. This window encapsulates the industrial spatial state information from time $t-T+1$ to t. In this paper, a graph structure is constructed for each time slice to represent the relational network among different spatial units. For time t, the graph structure is defined as:

where $\hat{Y}_{t+1}$ represents the model's predicted output of manufacturing industrial land use change results for each spatial unit at the next time step.

centred on the above task definition, this paper constructs a spatiotemporal prediction framework consisting of five

$$G_t = (V_t, E_t, A_t) \quad (3)$$

where V_t denotes the node set, E_t the edge set, and A_t the adjacency matrix. The node set corresponds to all spatial units within the study area, while the edge set reflects spatial adjacency, transportation linkage, and functional similarity between nodes. The graph structure sequence composed of multiple time slices can be denoted as:

$$\mathcal{A} = \{A_{t-T+1}, A_{t-T+2}, \dots, A_t\} \quad (4)$$

On this basis, the prediction objective of this paper can be formulated as learning a mapping function $f(\cdot)$ from the historical node feature sequence and adjacency relation sequence to the future manufacturing industrial land use change outcome, namely:

$$\hat{Y}_{t+1} = f(\mathcal{X}, \mathcal{A}) \quad (5)$$

components: a multi-source data input and spatiotemporal graph construction module, an input projection and feature fusion module [24], a graph attention-based spatial encoding module, a Transformer-based temporal evolution modelling module, and a prediction head and spatial decoding module. The overall model framework is illustrated in Figure 4.

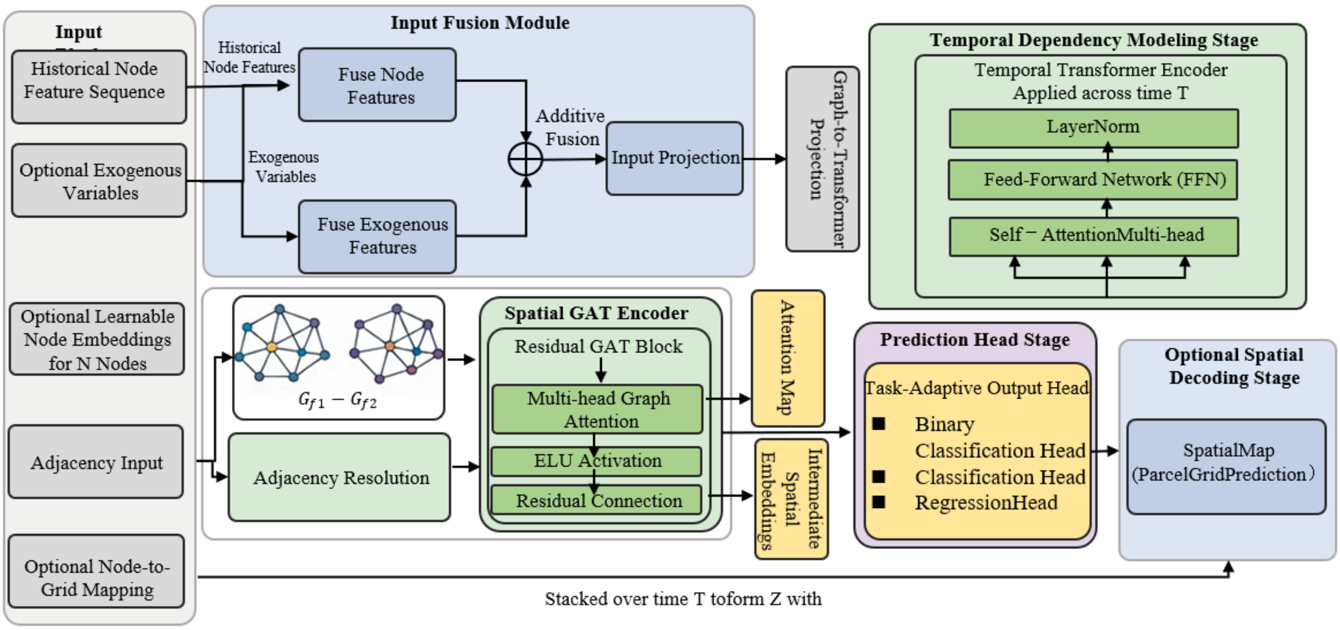

Figure 4. Model Structure Diagram

3.2. Spatiotemporal Graph Construction

The dynamic change of manufacturing industrial land depends not only on the attributes of the unit itself but also on the development status of surrounding areas and the spatial connection network [25]. To incorporate such complex spatial interaction mechanisms into a unified modelling framework, this paper abstracts the study area into a spatiotemporal graph structure. In this graph, each spatial unit corresponds to a node, and edges between nodes describe multiple relationships including spatial adjacency, transportation accessibility [26], and functional similarity. In this way, the traditional "region-attribute" representation in land use research can be extended to a "node-relation-attribute" graph representation, laying the foundation for subsequent graph neural network learning.

3.2.1. Spatial Adjacency Relation Construction

The expansion of manufacturing industrial land exhibits obvious local spillover characteristics. Especially at the boundaries of traditional manufacturing districts, around industrial parks, and along major transportation corridors, land-use changes between adjacent spatial units often present strong spatial linkage. Therefore, this paper first constructs the most fundamental spatial adjacency relationship. Two spatial units are regarded as spatially adjacent if they are geometrically directly contiguous or the distance between their centroids is smaller than a predefined threshold.

Let$d_{ij}^{(s)}$ denote the Euclidean distance or centroid distance between node i and node j. The spatial adjacency matrix can then be defined as:

$$A_{ij}^{(s)} = \begin{cases} 1, & d_{ij}^{(s)} \le \delta_s, i \ne j \\ 0, & \text{otherwise} \end{cases} \tag{6}$$

where δ_s is the spatial adjacency threshold. In the experiments, $d^{(s)}$ is set to 1.5 km. For parcel-based spatial units, a spatial edge is also retained when two units share a common boundary, even if their centroid distance exceeds the threshold. Matrix $A^{(s)}$ is mainly used to characterize the local spatial diffusion effect in manufacturing industrial land change.

3.2.2. Multi-relational Fused Adjacency Matrix

Considering that the dynamic changes of manufacturing industrial land use are not driven by a single spatial relationship, this paper constructs a unified adjacency matrix by weighted fusion of spatial adjacency, transportation accessibility, and functional similarity relationships. For time t, the fused adjacency matrix is defined as:

$$A_t = \alpha A_t^{(s)} + \beta A_t^{(r)} + \gamma A_t^{(f)} \tag{7}$$

where α, β, and γ denote the weight coefficients of the three types of relationships, satisfying:

$$\alpha + \beta + \gamma = 1, \alpha, \beta, \gamma \ge 0 \tag{8}$$

This weighting scheme unifies local spatial diffusion, transportation-oriented propagation, and functionally similar linkage into the same graph structure. Transportation edges are defined when the shortest road-network distance between two spatial units does not exceed 2.0 km, while functional-similarity edges are retained when the cosine similarity between their standardized POI and supporting-environment feature vectors is at least 0.80. The three externally constructed relations are fused using weights of 0.45, 0.35, and 0.20 for spatial adjacency, transportation connectivity, and functional similarity, respectively. If the graph structure changes slightly during the study period, a static graph can be adopted; when the transportation network, functional pattern [27], or spatial organization varies significantly across time slices, the adjacency matrix at each time step is constructed separately to form a dynamic graph sequence.

Furthermore, to further enhance the model's ability to learn potential implicit relationships, this paper also allows the adaptive generation of a learnable dynamic adjacency matrix based on node features after input projection. Let the projected node representation be $H_t^{(0)}$; the dynamic adjacency matrix can be defined as:

$$Q_t = H_t^{(0)} W_Q, K_t = H_t^{(0)} W_K \tag{9}$$

$$A_t^{(d)} = \text{softmax}\left(\frac{Q_t K_t^{\top}}{\sqrt{d}}\right) \tag{10}$$

where $A_t^{(d)}$ denotes the dynamic adjacency matrix generated based on feature correlation, and d is the feature dimension. Finally, it can be fused with the externally constructed adjacency matrix:

$$\tilde{A}_t = \lambda A_t + (1 - \lambda) A_t^{(d)} \tag{11}$$

where λ the adaptive-adjacency coefficient is set to 0.25. This design enables the mining of potential high-order correlations among nodes beyond explicit spatial relationships.

3.3. Spatial Dependency Learning Based on Graph Attention Network

3.3.1. Introduction of Graph Attention Mechanism

Traditional graph convolutional networks perform neighbourhood feature aggregation through normalized adjacency matrices, which essentially assume that the contribution of each neighbouring node is relatively balanced within the local scope. However, the dynamic change of manufacturing industrial land exhibits significant spatial heterogeneity [28-29], and not all neighbours exert equal influence on the central node.

To enhance the model's expressive capacity for complex spatial relationships, a multi-head attention mechanism is adopted in the graph attention layer. Let the number of attention heads be K; the k-th head corresponds to a set of independent parameters $W^{(k)}$ and $\alpha^{(k)}$, and computes a separate set of neighborhood attention weights. For intermediate layers, the outputs of multiple heads are obtained by concatenation:

$$h_i' = \Vert_{k=1}^{K} \sigma\left(\textstyle\sum_{j \in \mathcal{N}(i)} \alpha_{ij}^{(k)} W^{(k)} h_j\right) \tag{12}$$

where ‖ denotes vector concatenation. This design enables the learning of spatial dependencies from distinct feature subspaces, improving the model's ability to represent complex neighborhood patterns. At the output layer, to control dimensionality and enhance stability, the results of multiple attention heads can be fused via averaging or linear mapping, namely:

$$z_i = \frac{1}{K} \sum_{k=1}^{K} \sigma\left(\textstyle\sum_{j \in \mathcal{N}(i)} \alpha_{ij}^{(k)} W^{(k)} h_j\right) \tag{13}$$

where z_i denotes the spatial embedding of node i at time t.

3.3.2. Residual Graph Attention Encoding Block

Considering that deeper graph neural networks may suffer from representation degradation, information loss, or difficult gradient propagation during training [30], this paper further adds Dropout, residual connection, and LayerNorm after each graph attention block to form a residual graph attention encoding block. For the input $H_t^{(l)}$of the l layer, its output can be expressed as:

$$\bar{H}_t^{(l+1)} = \text{Dropout}\left(\text{GAT}(H_t^{(l)}, A_t)\right) \tag{14}$$

$$H_t^{(l+1)} = \text{LayerNorm}\left(H_t^{(l)} + \bar{H}_t^{(l+1)}\right) \tag{15}$$

where GAT(·) denotes the aggregation result of the graph attention layer. Residual connections help preserve the original node representations and avoid over-smoothing caused by deep networks; LayerNorm is used to stabilize the feature distribution during training. After L_g layers of graph attention encoding, the final spatial embedding at time t is denoted as:

$$Z_t = H_t^{(L_g)} \in \mathbb{R}^{N \times d_g} \tag{16}$$

3.3.3. Temporal Aggregation and Prediction Head

After graph attention encoding, the spatial embeddings within the historical observation window are arranged as a temporal sequence and input into the Transformer encoder. The Transformer consists of two encoding layers with a 128-dimensional input, four attention heads, a 256-dimensional feed-forward network, and a dropout rate of 0.10. Positional encoding preserves temporal order, while multi-head self-attention captures dependencies across historical periods. The resulting sequence is then aggregated into a node-level representation for next-step manufacturing industrial land change prediction.
aggregation. Last-step aggregation only retains the representation of the most recent time slice, while mean aggregation takes the equal-weighted sum of all time slices:

$$h_i = \frac{1}{T} \sum_{\tau=1}^{T} H_{\tau,i} \tag{17}$$

In contrast, attention-based aggregation allows the model to automatically learn the importance of different historical periods. Given that the contributions of different stages to future changes are inconsistent in the evolution of manufacturing industrial land use, this paper adopts attention-based aggregation as the primary scheme. Specifically, the importance score for the representation of each time slice is first calculated:

$$s_{\tau,i} = w^\top H_{\tau,i} + b \tag{18}$$

The scores are then normalized to temporal weights via softmax:

$$\omega_{\tau,i} = \frac{\exp(s_{\tau,i})}{\sum_{m=1}^{T} \exp(s_{m,i})} \tag{19}$$

$$h_i = \sum_{\tau=1}^{T} \omega_{\tau,i} H_{\tau,i} \tag{20}$$

where $\omega_{\tau,i}$ denotes the importance of the τ-th time slice for the prediction task of node I. This design enables the model to automatically highlight the historical stages that are most discriminative for future manufacturing conversion.

Up to this point, the spatial dependency information of nodes at each time slice has been encoded into high-level representations, providing input for subsequent temporal evolution modelling.

Common aggregation strategies include last-step aggregation, mean aggregation, and attention-based
After obtaining the node-level spatiotemporal fused representation h_i , this paper employs a multi-layer perceptron (MLP) as the prediction head. For multi-class classification tasks, the prediction head outputs a C-dimensional vector:

$$= W_c h_i + b_c \tag{21}$$

$$p_{ic} = \frac{\exp(o_{ic})}{\sum_{m=1}^{C} \exp(o_{im})} \tag{22}$$

$$\hat{y}_i = W_r h_i + b_r \tag{23}$$

Class probabilities are computed via Softmax. For continuous-value prediction tasks, regression values are directly output. The model can generate binary classification, multi-class classification, or regression results according to the specific task formulation.

3.4. Spatial Decoding Module

The direct output of the spatiotemporal predictor is a node-level probability, class label, or continuous value. Although node-level outputs are suitable for quantitative evaluation, they are less intuitive for industrial land planning and spatial analysis [31]. The spatial decoding module therefore remaps each node prediction to its corresponding geographic spatial unit, generating manufacturing industrial land conversion probability maps, classified distribution maps, hotspot maps, or continuous change-intensity maps. The schematic procedure is shown in Figure 5.
Let the node-level prediction results be denoted as:

$$\hat{Y}_{node} = \{\hat{y}_1, \hat{y}_2, \dots, \hat{y}_N\} \tag{24}$$

When parcel-based spatial units are adopted, the spatial decoding process can be formulated as: $\hat{Y}_{map}(P_i) = \hat{Y}_{node}(i)$ (25)

where P_i represents the parcel polygon corresponding to node i. This mapping process essentially leverages the one-to-one correspondence between nodes and spatial units to restore the model outputs to the original geographic space.

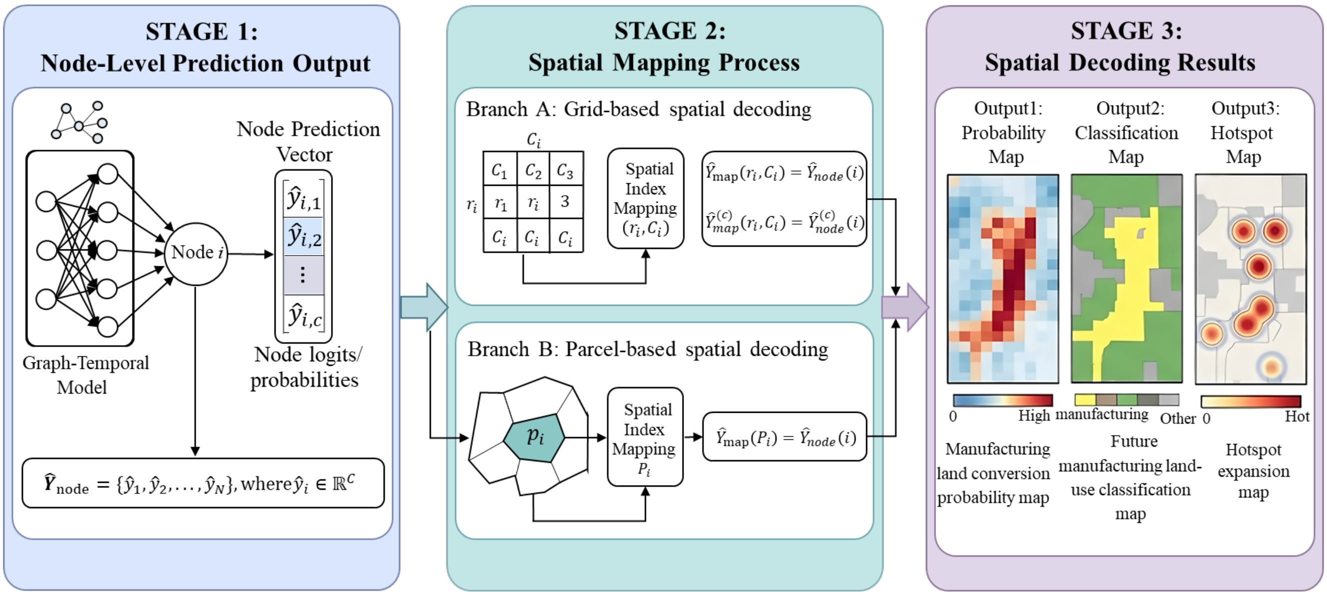

Figure 5. Principle Diagram of Spatial Decoding Module

The spatial decoding module is an output-space mapping rather than a feature-learning component: it does not change the node-level logits, probabilities, or regression values produced by the predictor. Its contribution is to restore the one-to-one correspondence between model outputs and geographic units, thereby enabling spatial-consistency evaluation, map-based comparison, hotspot identification, and planning-oriented interpretation. Accordingly, improvements in node-level predictive accuracy are attributed to the spatiotemporal predictor rather than directly to the spatial decoder.

3.5. Loss Function

Since the method proposed in this paper can be applied to binary classification prediction and extended to multi-class classification and continuous-value prediction, the loss function is configured correspondingly according to the task formulation. For binary classification tasks, let the ground-truth label be $y_i \in \{0,1\}$ and the conversion probability output by the model be p_i. Binary cross-entropy loss is employed:

$$L_{cls} = -\frac{1}{N}\sum_{i=1}^{N} [y_i \log p_i + (1-y_i)\log(1-p_i)] \quad (26)$$

This loss function directly measures the discrepancy between predicted probabilities and ground-truth labels and is the most commonly used objective function in binary classification tasks.

For regression tasks, if the prediction target is the manufacturing industrial land use ratio, intensity change, or continuous development potential value, mean squared error loss is adopted:

$$L_{reg} = \frac{1}{N}\sum_{i=1}^{N} (y_i - \hat{y}_i)^2 \quad (27)$$

In the main experiments of this paper, the model is mainly used for manufacturing industrial land conversion identification, so binary classification loss is primarily adopted. During training, the graph attention network, Transformer, prediction head, and related projection parameters are jointly optimized by minimizing the loss function, enabling the model to gradually learn the spatiotemporal evolutionary patterns underlying the dynamic changes of manufacturing industrial land use.

4. Experimental Design and Evaluation Methods

To evaluate the proposed framework for dynamic manufacturing industrial land prediction, the experiments are organized around four aspects: temporal data partitioning and training settings, comparison with baseline models, quantitative evaluation, and spatial visualization of prediction results.

4.1. Experimental Data Organization and Sample Partitioning

This paper constructs a manufacturing industrial land dynamic change sample set based on multi-period land-use and multi-source industrial spatial data of a city from 2014 to 2023. The source database retains the underlying temporal observations at month-level granularity before annual aggregation, making it possible to organize the study period at two temporal scales. The primary model comparison and spatial-consistency experiments use annual samples. Considering that this task is a typical time-series prediction problem, random shuffling is not adopted; instead, the training, validation, and test sets are strictly organized in chronological order to avoid future-information leakage. Specifically, samples from 2014 to 2019 are used for model training, those from 2020 to 2021 for parameter tuning and early stopping control, and those from 2022 to 2023 for final testing. The proportions of the training, validation, and test sets are 60%, 20%, and 20%, respectively.

For the primary annual-scale temporal modelling task, a historical observation window of length 4 is used as input: node features and graph structures from four consecutive annual periods are used to predict the manufacturing industrial land outcome of the subsequent annual period. This setting preserves long-term evolution information while controlling model complexity.

In addition, a supplementary monthly-resolution experiment is constructed from the retained month-level records to evaluate short-term temporal dynamics. The same GAT-Transformer architecture and graph-construction rules are used, while the temporal step is redefined as one month; therefore, T = 4 corresponds to four consecutive months in this auxiliary experiment. The chronological split remains 2014–2019 for training, 2020–2021 for validation, and 2022–2023 for testing. Consequently, the monthly analysis reported in Section 5.5.2 does not alter the annual-scale primary experimental results. The detailed temporal partitioning and dual-scale sample construction settings are summarized in Table 1.

Table 1. Temporal Data Partitioning and Dual-scale Sample Construction Settings

Item	Setting
Study Area	The main manufacturing areas and key industrial expansion zones of a city
Time Span	2014–2023
Temporal Resolution	Annual
Supplementary Temporal Resolution	Monthly
Primary Annual Historical Input Window	4 annual periods
Supplementary Monthly Historical Window	4 months
Prediction Target	Predict manufacturing industrial land-use change at the next time step
Sample Construction Method	Predict the 5th-period manufacturing industrial land-use change using 4 consecutive periods of spatiotemporal features
Training Set Time Range	2014–2019
Validation Set Time Range	2020–2021
Test Set Time Range	2022–2023
Training Set Ratio	60%
Validation Set Ratio	20%
Test Set Ratio	20%

4.2. Parameter Settings and Training Environment

The model is implemented using the PyTorch framework, and all training and testing processes are completed in a unified experimental environment. The experimental platform is an NVIDIA GeForce RTX 4070 12GB GPU. All comparative models are trained and tested under the same data partitioning and consistent evaluation metrics to ensure comparability. The supplementary monthly-resolution experiment uses the same network architecture, graph-construction settings, optimizer, and regularization configuration as the annual model; only the temporal unit of the input sequence is changed from years to months. The specific parameter settings are listed in Table 2.

Table 2. Model Training Parameters and Operating Environment Setting

Parameter Category	Parameter Name	Setting Value
Input Parameters	Node Feature Dimension	16
Historical Time Window Length	primary annual model	4 annual periods
Historical Time Window Length	supplementary monthly experiment	4 months
Graph Encoding	GAT Hidden Dimension	64
Graph Encoding	Graph Embedding Dimension	128
Graph Encoding	Number of GAT Layers	2
Graph Encoding	Number of Attention Heads	4
Graph Encoding	Graph Encoding Dropout	0.10
Temporal Encoding	Transformer Input Dimension	128
Temporal Encoding	Feed-forward Hidden Dimension	256
Temporal Encoding	Number of Transformer Layers	2
Temporal Encoding	Number of Multi-Head Attention Heads	4
Temporal Encoding	Transformer Dropout	0.10
Aggregation	Temporal Aggregation Method	Attention Pooling
Output Parameters	Output Type	Binary/multi-class classification/regression
Optimization	Optimizer	Adam
Optimization	Initial Learning Rate	0.001
Optimization	Weight Decay	1e-4
Optimization	Batch Size	32
Optimization	Training Epochs	600
Optimization	Gradient Clipping Threshold	5.0
Hardware Environment	GPU	NVIDIA GeForce RTX 4070 12GB
Hardware Environment	Deep Learning Framework	PyTorch

4.3. Evaluation Metrics

Evaluation is conducted for three task formulations. For binary conversion classification and six-class transition classification, node-level performance is evaluated using

Accuracy, Precision, Recall, and F1-score. Spatial consistency between predicted and observed geographic patterns is evaluated using Kappa, Figure of Merit (FoM), and intersection-over-union measures. For continuous manufacturing industrial land change-intensity regression, MAE, RMSE, R^2, and Pearson's r are adopted to evaluate prediction error, goodness of fit, and linear correlation between predicted and observed values. The definitions of the main evaluation metrics are summarized in Table 3.

Table 3. Definition of Evaluation Indicators

Indicator	Formula	Explanation of meaning
Accuracy	$Accuracy = \frac{TP+TN}{TP+TN+FP+FN}$	Indicates the overall classification accuracy, which measures the model's overall ability to correctly identify all samples.
Precision	$Precision = \frac{TP}{TP+FP}$	Represents the proportion of true positive samples among those predicted as manufacturing industrial land conversion, reflecting the reliability of the model's predictions.
Recall	$Recall = \frac{TP}{TP+FN}$	Represents the proportion of true manufacturing industrial land conversion samples that are correctly identified, reflecting the model's ability to detect changed samples.
F1-score	$F1 = \frac{2 \times Precision \times Recall}{Precision + Recall}$	The harmonic mean of Precision and Recall, suitable for imbalanced classification tasks.
Kappa	$Kappa = \frac{P_o - P_e}{1 - P_e}$	Measures the agreement between predicted and actual results beyond random chance.
FoM	$FoM = \frac{B}{A+B+C+D}$	An indicator for evaluating the prediction accuracy of changed areas, where (B) denotes the correctly predicted changed regions.
IoU	$IoU = \frac{TP}{TP+FP+FN}$	Measures the spatial overlap between predicted and actual changed areas.
Loss	Optimizing the objective function value during the training process	Used to reflect the convergence status during model training.

5. Experimental Results and Analysis

5.1. Model Training Process and Convergence Analysis

Figure 6 illustrates the variation of Loss, Kappa, Accuracy, and RMSE during model optimization. The curves shown during training correspond to the training and validation sets; the held-out 2022–2023 test period is reserved for final evaluation and is not used for epoch-by-epoch model monitoring. The training and validation curves follow consistent overall trends, indicating a stable optimization process without obvious divergence.

Both training loss and validation loss decrease rapidly during the early epochs and gradually stabilize after approximately 200 epochs. Kappa and Accuracy increase during the same period and then approach stable plateaus. The validation curves remain slightly below the training curves while following similar trends, indicating a limited generalization gap during model selection without using the held-out test set for monitoring.

The RMSE curves also decrease sharply during the initial stage and remain at a relatively low and stable level thereafter. Overall, the training-validation curves indicate satisfactory convergence and optimization stability. Final generalization performance is assessed separately on the held-out test period.

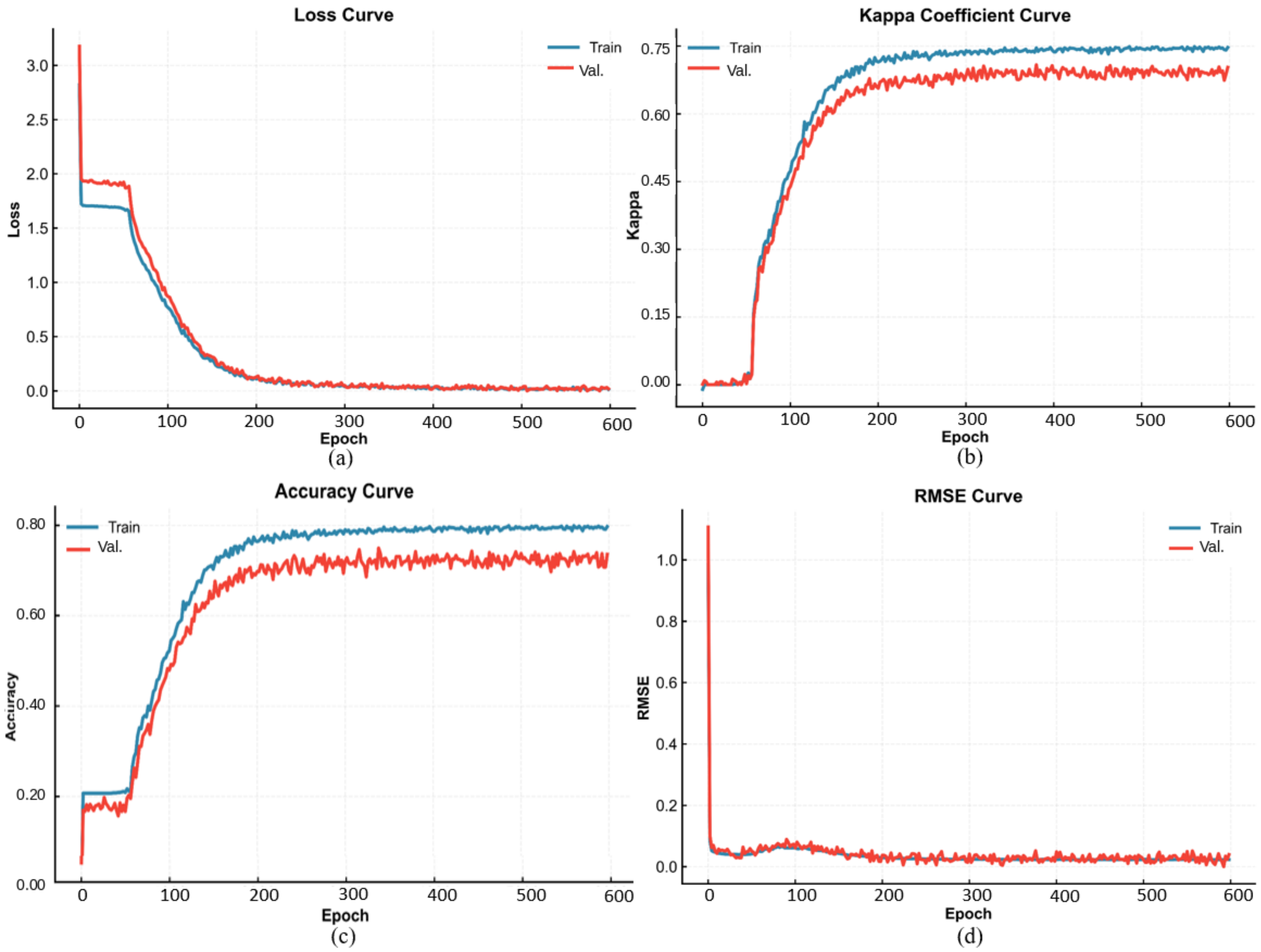

Figure 6. Training and validation curves for Loss, Kappa, Accuracy, and RMSE

5.2. Node-Level Classification Result Analysis of Different Models

Table 4 reveals distinct hierarchical differences among various models in the node-level manufacturing industrial land change identification task: traditional machine learning models perform the weakest, followed by sequential models and graph structure models in ascending order, and spatiotemporal joint models achieve the best performance. This indicates that manufacturing industrial land changes possess both spatial dependence and temporal evolution characteristics, and single-dimension modelling is insufficient to characterize their complex patterns.

Among traditional machine learning models, Logistic Regression achieves the lowest performance, while Random Forest and XGBoost provide moderate improvements but still lack explicit spatial and temporal dependency modelling. Among graph-based models, GAT performs better than GCN, which is consistent with its ability to assign heterogeneous weights to neighbouring spatial units. Among spatiotemporal joint models, GCN-Transformer reaches an Accuracy of 0.751 and a Macro-F1 of 0.692, while the proposed GAT-Transformer-Spatial Decoder framework achieves the best Accuracy of 0.768 and Macro-F1 of 0.712. Relative to GCN-Transformer, the gains of 0.017 in Accuracy and 0.020 in Macro-F1 support the benefit of attention-based spatial encoding under a comparable temporal modelling backbone. The spatial decoder is used for geographic remapping and is not interpreted as the direct source of node-level classification gains.

As shown in Figure 7, the overall performance trend across evaluation metrics is consistent with Table 4. Accuracy and Weighted-F1 are generally higher than Macro-Recall and

Macro-F1, indicating that class imbalance and the difficulty of identifying changed samples remain important challenges. Nevertheless, the proposed framework maintains the strongest overall performance across the reported metrics.

Table 4. Comparison of Node-level Classification Results of Different Models

Model	Accuracy	Macro-Precision	Macro-Recall	Macro-F1	Weighted-F1
Logistic Regression	0.612	0.541	0.498	0.514	0.586
Random Forest	0.646	0.583	0.536	0.554	0.621
XGBoost	0.663	0.601	0.553	0.572	0.639
LSTM	0.689	0.634	0.589	0.607	0.668
GCN	0.712	0.662	0.621	0.637	0.694
GAT	0.724	0.678	0.639	0.654	0.708
GCN-Transformer	0.751	0.713	0.681	0.692	0.739
GAT-Transformer-Spatial Decoder	**0.768**	**0.724**	**0.701**	**0.712**	**0.756**

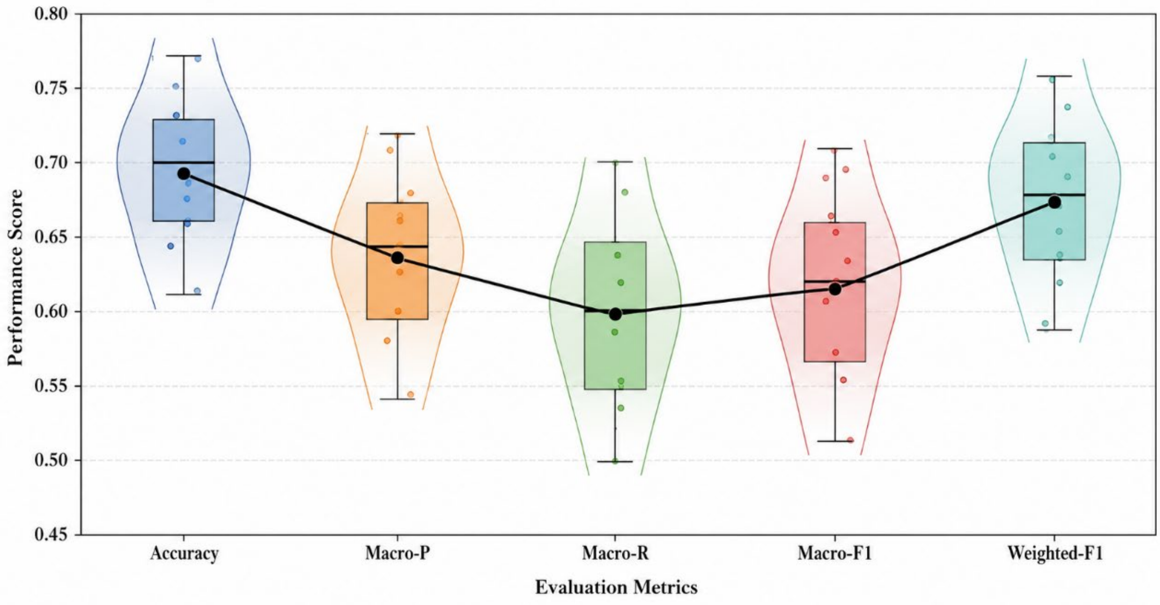

Figure 7. Box plot comparing node-level classification results of different models

5.3. Spatial Consistency Evaluation of Different Models

Figure 8 compares the spatial consistency of different models and shows a clear performance hierarchy. Traditional machine learning models perform weakest because they do not explicitly represent relationships among spatial units; Logistic Regression records an FoM of 0.201 and an mIoU of 0.318. Random Forest and XGBoost improve these results, with XGBoost reaching a Kappa of 0.531 and an mIoU of 0.361, but their ability to reproduce continuous spatial change patterns remains limited.

Spatiotemporal joint modelling further improves spatial consistency. GCN-Transformer reaches a Kappa of 0.654 and an mIoU of 0.473, whereas the proposed framework achieves a Kappa of 0.668, FoM of 0.351, and mIoU of 0.498. Compared with GCN-Transformer, Kappa increases by 0.014 and mIoU by 0.025. These improvements reflect the stronger spatiotemporal predictive representation; the spatial decoder provides geographic mapping for visualization and spatial evaluation but does not modify the underlying node predictions.

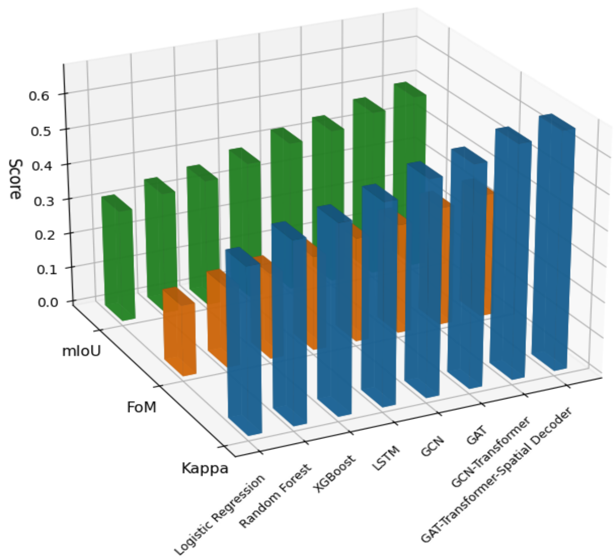

Figure 8. Comparison of Spatial Consistency Performance Across Models

5.4. Multi-Class Classification and Regression Performance Analysis of Manufacturing Industrial Land Change

5.4.1. Multi-Class Manufacturing Industrial Land Classification Result Analysis

Figure 9 presents the confusion matrix of the proposed GAT-Transformer-Spatial Decoder model for the six-class transition task. Persistent non-manufacturing and persistent manufacturing samples are concentrated on the main diagonal, indicating stable recognition of relatively mature land states. Most errors occur among transition categories, which is consistent with the gradual and boundary-ambiguous nature of manufacturing land evolution. Overall, the confusion matrix supports the model's ability to distinguish both stable states and complex transition patterns.

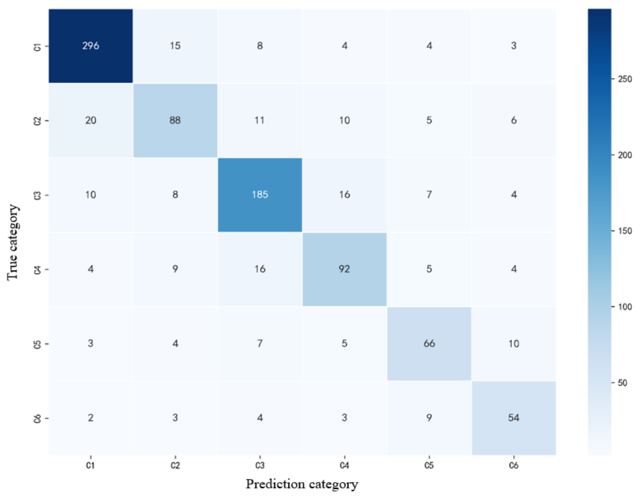

Figure 9. Confusion Matrix of Model 6 Classification

Table 5 and Figure 10 display the classification performance differences of the main model across each category. In general, the model's identification performance on stable categories is significantly superior to that on change categories, with Category C1 (persistent non-manufacturing) and Category C3 (persistent manufacturing) achieving the best results, with F1-scores of 0.881 and 0.778 respectively. This indicates that the model can accurately learn the feature patterns and spatial distribution rules of categories with relatively stable manufacturing states and large sample sizes.

In contrast, change samples pose greater identification challenges. Category C2 (conversion to manufacturing) obtains the lowest F1-score of 0.632 among all categories, suggesting that the identification of newly added manufacturing industrial land remains a major challenge. From the comparison between Precision and Recall, certain differences exist among different change categories. The Recall of C2 is relatively low, indicating room for improvement in the model's ability to detect newly added manufacturing samples; while the Recall of C6 is higher than Precision, showing that the model is sensitive to manufacturing land exit areas but accompanied by certain misjudgements. Overall, the Macro Average Precision, Recall, and F1-score of the main model all reach 0.719, demonstrating its balanced classification performance in the multi-class manufacturing industrial land change identification task, while also reflecting that change samples remain the focus for subsequent optimization.

Table 5. Classification Performance of Various Categories of the Main Model

Category	Precision	Recall	F1-score
C1 Non-manufacturing	0.877	0.885	0.881
C2 Transfer to Manufacturing	0.659	0.607	0.632
C3 Persistent Manufacturing	0.773	0.783	0.778
C4 Manufacturing Development Upgrade	0.674	0.685	0.679
C5 Manufacturing Development Decline	0.670	0.663	0.667
C6 Transfer out of Manufacturing	0.658	0.693	0.675
Macro Average	**0.719**	**0.719**	**0.719**

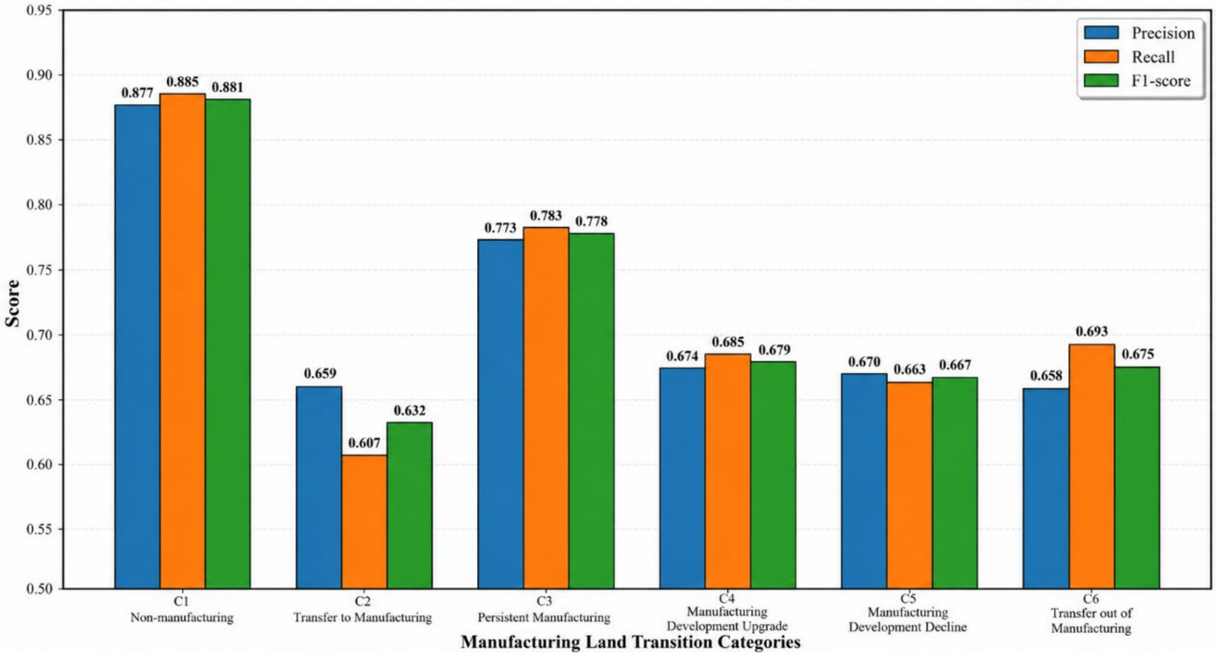

Figure 10. Bar chart showing the classification performance of each category of the main model

5.4.2. Comparison of Regression Performance for Manufacturing Industrial Land Change Intensity

As shown in Table 6 of the regression task results, significant performance differences exist among different models in predicting manufacturing industrial land change intensity. Traditional machine learning methods exhibit relatively weak overall performance. Specifically, Logistic Regression achieves MAE and RMSE values of 0.132 and 0.168, respectively, with R^2 and Pearson r of only 0.421 and 0.672, indicating that linear models are insufficient to characterize the complex nonlinear relationships inherent in the process of manufacturing industrial land change.

Spatiotemporal joint models achieve the best performance. GCN-Transformer further reduces MAE and RMSE to 0.081 and 0.102, respectively, and increases R^2 and Pearson r to 0.748 and 0.871. In contrast, the model proposed in this paper attains optimal performance across all four metrics, with MAE and RMSE of 0.077 and 0.097, and R^2 and Pearson r reaching 0.765 and 0.881, respectively. The results demonstrate that the proposed model possesses higher fitting accuracy and correlation in manufacturing industrial land change intensity prediction, enabling more effective joint utilization of spatial dependence information and temporal evolution patterns.

Table 6. Task Performance Indicators of Different Models

Model	MAE	RMSE	R^2	Pearson r
Logistic Regression	0.132	0.168	0.421	0.672
Random Forest	0.118	0.149	0.516	0.731
XGBoost	0.109	0.138	0.573	0.758
LSTM	0.098	0.124	0.647	0.812
GCN	0.091	0.116	0.691	0.836
GAT	0.087	0.109	0.723	0.851
GCN-Transformer	0.081	0.102	0.748	0.871
Ours	**0.077**	**0.097**	**0.765**	**0.881**

5.5 Regression Performance and Spatiotemporal Analysis of Manufacturing Industrial Land Change Intensity

5.5.1. Comparative Analysis of Regression Fitting Results of Different Models

Figure 11 illustrates the scatter distributions of predicted versus observed values for the proposed model, Random Forest, GCN, and LSTM in the regression task. All models can capture the relationship between manufacturing industrial land change intensity and the observed values to a certain extent. However, distinct differences exist among the models in terms of scatter clustering, dispersion degree, and the proximity of the fitting line to the ideal line.

The scatter distribution of the proposed model is the most concentrated, with the minimal deviation between the fitting line and the ideal line, and most sample points cluster near the ideal line, indicating that the model achieves the most stable fitting of the true value variation trend with overall small prediction errors. In comparison, Random Forest exhibits the most dispersed scatter distribution, with significant deviations especially in the medium-to-high value range, implying its relatively limited capability in fitting complex continuous change relationships. The performances of GCN and LSTM fall in between, with GCN showing superior scatter clustering over LSTM, demonstrating that explicit incorporation of spatial relationships enhances the stability of regression prediction. Although LSTM can utilize time-series information, it still suffers from obvious dispersion and underestimation in certain sample intervals.

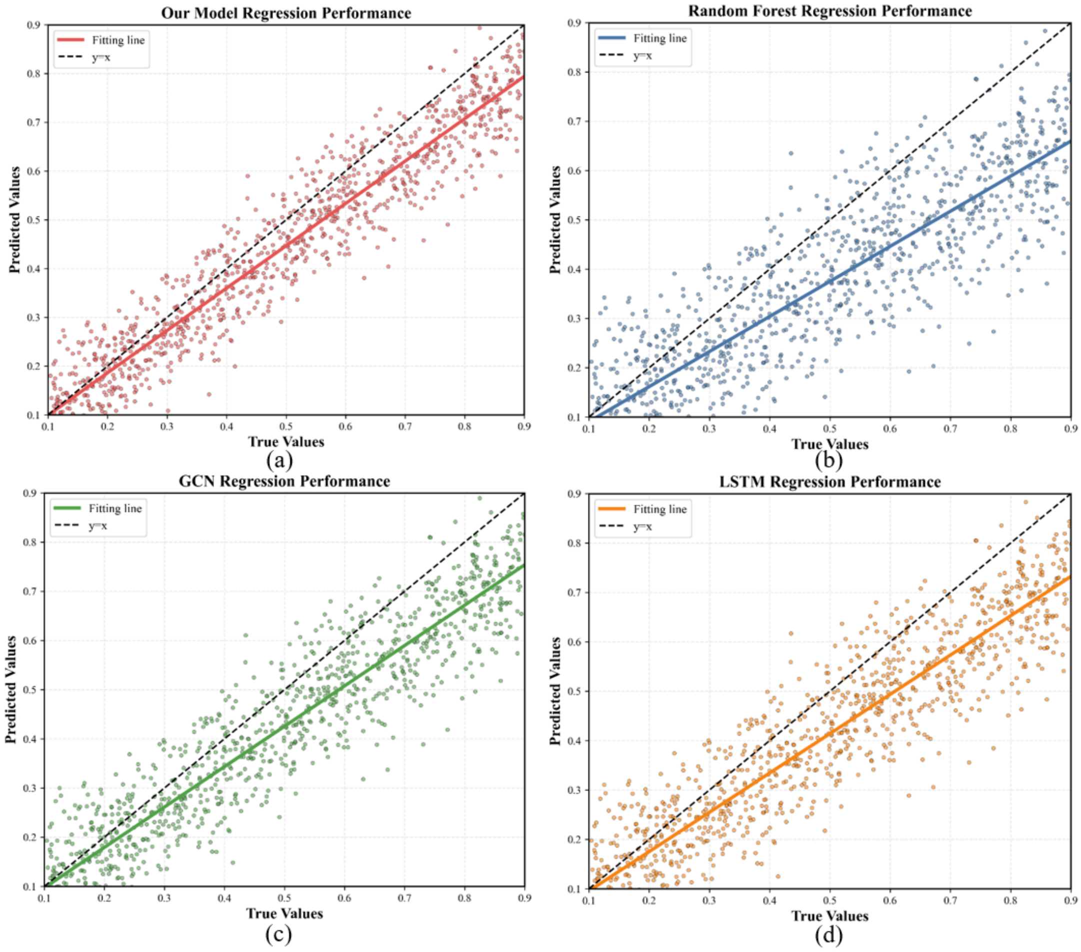

Figure 11. Scatter plot of predictions from different models

5.5.2. Component-wise Ablation Analysis

To further investigate the contribution of the main components in the proposed framework, a component-wise ablation experiment is conducted on the same training, validation, and test partitions used in the primary task. The results are summarized in Table 7. Removing the adaptive adjacency component or retaining only the spatial adjacency relation results in decreases in both classification and regression performance, indicating that learnable implicit relations and multi-relational graph fusion provide complementary information. Replacing GAT with GCN also reduces performance, demonstrating the benefit of assigning heterogeneous attention weights to neighbouring spatial units. Removing the Transformer temporal encoder produces the largest performance degradation among the predictive components, confirming the importance of temporal dependency modelling. In contrast, removing the spatial decoding module does not change node-level classification or regression metrics but eliminates direct geographic map outputs, which is consistent with its role as an output-space mapping and interpretation module rather than a predictive feature-learning component

Table 7. Component-wise Ablation Results

Model variant	Accuracy	Macro-F1	MAE	R^2
Full model	0.768	0.712	0.077	0.765
Without adaptive adjacency	0.761	0.703	0.080	0.753

Model variant	Accuracy	Macro-F1	MAE	R²
Spatial adjacency only	0.754	0.695	0.083	0.742
GCN replacing GAT	0.751	0.692	0.081	0.748
Without Transformer temporal encoder	0.732	0.661	0.089	0.714
Without spatial decoder	0.768	0.712	0.077	0.765

5.5.3 Supplementary Monthly-scale Temporal Prediction Analysis of Manufacturing Industrial Land Change Intensity

To examine short-term temporal variations, a supplementary monthly-resolution experiment was conducted using the original monthly records. The same GAT-Transformer architecture and graph-construction rules were adopted, with each temporal step representing one month and T=4 corresponding to four consecutive months. The data split remained unchanged (2014–2019 training, 2020–2021 validation, and 2022–2023 testing). As shown in Figure 12, the predicted monthly change intensity from December 2021 to December 2023 closely follows the observed trend and captures most short-term fluctuations.

The prediction intervals remain narrow and stable, including during higher-intensity periods such as October 2022 and August 2023. Overall, the model demonstrates stable monthly prediction performance under different fluctuation conditions.

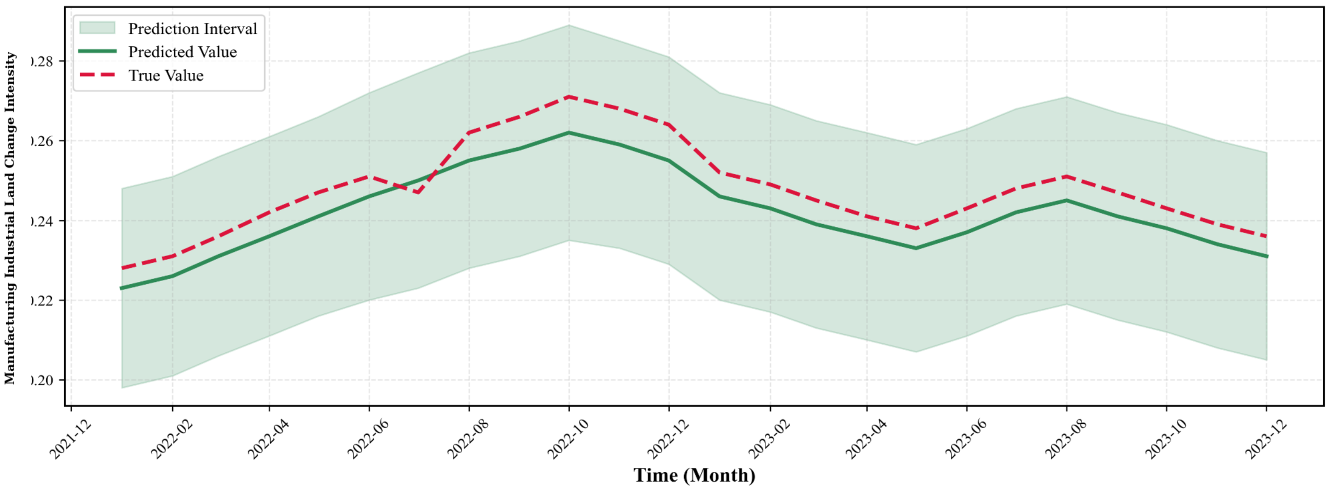

Figure 12. Supplementary Monthly-scale Temporal Prediction Analysis of Manufacturing Industrial Land Change Intensity

5.5.4 Spatial Distribution Analysis of Manufacturing Industrial Land Change Intensity

Figure 13 compares the observed and predicted spatial distributions of manufacturing industrial land change intensity. The two heatmaps show a similar overall pattern, with high-intensity areas concentrated in the main manufacturing cluster and nearby development zones, while lower-intensity areas are more common toward the periphery. Several smaller hotspots also appear along major transportation corridors and around local industrial nodes, suggesting that these locations may be undergoing active land-use adjustment or expansion. At a finer scale, the predicted map reproduces most of the main hotspots and spatial gradients found in the observed data. The agreement is particularly clear in the core manufacturing area and its surrounding zones, where the model captures both the location and relative intensity of major changes. Some medium- and low-intensity areas in the outer parts of the study region are also reflected in the predictions. Overall, the results indicate that the model can represent the main spatial pattern of manufacturing industrial land change, although local differences remain in several peripheral areas.

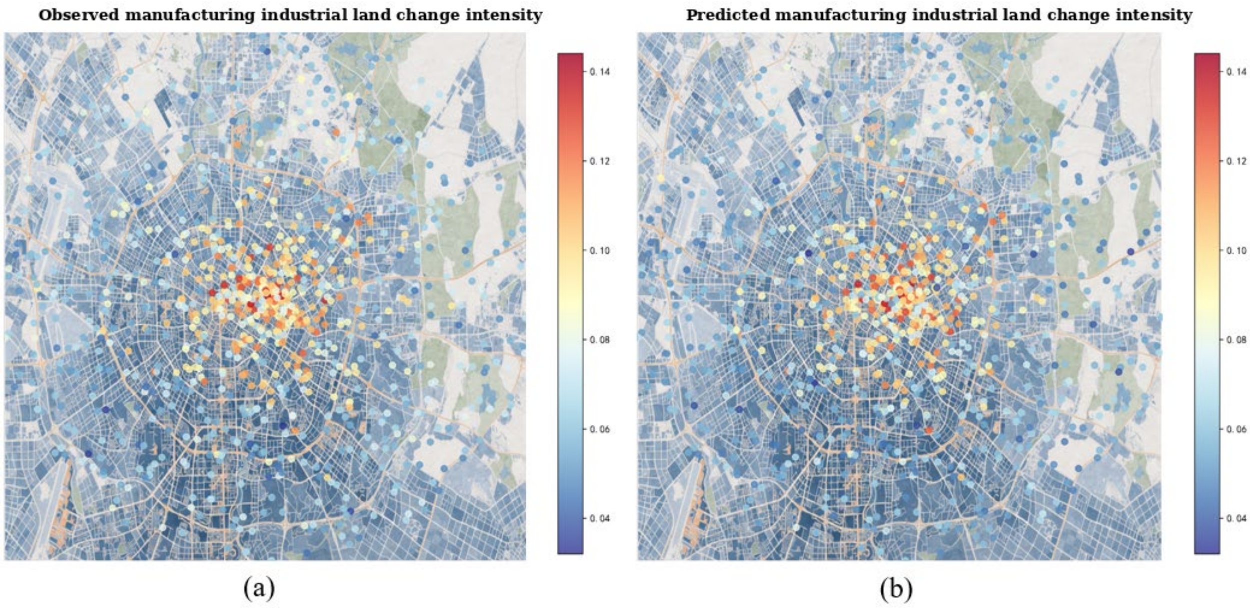

Figure 13. Heat maps of observed and predicted manufacturing industrial land change intensity

6. Conclusion

This study proposes a framework for manufacturing industrial land change prediction by integrating multi-relational graph construction, GAT-based spatial encoding, Transformer-based temporal modelling, and geographic spatial decoding. By organizing historical multi-source observations as a spatiotemporal graph, the framework jointly captures spatial relationships and temporal evolution. Compared with machine-learning, sequential, graph, and spatiotemporal baselines, it achieves the best overall performance in node-level classification, spatial consistency, and change-intensity regression.

The main methodological contribution lies in the task-specific integration of graph-attention and temporal-attention mechanisms. The spatial decoder maps node-level predictions back to geographic units for spatial interpretation without altering the predictive representation. In addition, a supplementary monthly-resolution experiment based on the original month-level records confirms the model's ability to capture short-term variations during the 2022–2023 test period.

Ablation results show that multi-relational graph construction, adaptive adjacency learning, GAT spatial encoding, and Transformer temporal encoding all contribute to performance, with the removal of the Transformer causing the largest degradation. Removing the spatial decoder does not affect node-level metrics, confirming its role in geographic visualization and interpretation. Future work will evaluate the framework across additional cities and regions to examine its generalizability under different industrial structures and data conditions.

Acknowledgements

This research was supported by the Science Foundation of Ministry of Education of China (Youth Program) under Grant number 20YJC760054.

Author contributions

Yuxuan, Hu: investigation, formal analysis, writing-review and editing. Yinan, Lin: conceptualization, supervision, writing-original draft, writing-review editing.

Data Availability Statement

The datasets and source code supporting the results of this study are available from the corresponding author upon reasonable request.

References

[1] Lee J, Davari H, Singh J, et al. Industrial Artificial Intelligence for industry 4.0-based manufacturing systems[J]. Manufacturing Letters, 2018, 18: 20-23.
[2] Leng J, Zhu X, Huang Z, et al. Unlocking the power of industrial artificial intelligence towards Industry 5.0: Insights, pathways, and challenges[J]. Journal of Manufacturing Systems, 2024, 73: 349-363.
[3] Mansour S, Al-Belushi M, Al-Awadhi T. Monitoring land use and land cover changes in the mountainous cities of Oman using GIS and CA-Markov modelling techniques[J]. Land use policy, 2020, 91: 104414.
[4] Verburg P H, Soepboer W, Veldkamp A, et al. Modeling the spatial dynamics of regional land use: the CLUE-S model[J]. Environmental management, 2002, 30(3): 391-

405.
[5] Xu L, Liu X, Tong D, et al. Forecasting urban land use change based on cellular automata and the PLUS model[J]. Land, 2022, 11(5): 652.
[6] Kuang W, Liu J, Dong J, et al. The rapid and massive urban and industrial land expansions in China between 1990 and 2010: A CLUD-based analysis of their trajectories, patterns, and drivers[J]. Landscape and Urban Planning, 2016, 145: 21-33.
[7] Zhang S, Li C, Ma Z, et al. Influences of different transport routes and road nodes on industrial land conversion: A case study of Changchun City of Jilin Province, China[J]. Chinese Geographical Science, 2020, 30(3): 544-556.
[8] Wang J, Hadjikakou M, Hewitt R J, et al. Simulating large-scale urban land-use patterns and dynamics using the U-Net deep learning architecture[J]. Computers, Environment and Urban Systems, 2022, 97: 101855.
[9] Niu H, Silva E A. Delineating urban functional use from points of interest data with neural network embedding: A case study in Greater London[J]. Computers, Environment and Urban Systems, 2021, 88: 101651.
[10] Ren Y, Xie Z, Zhai S. Urban land use classification model fusing multimodal deep features[J]. ISPRS International Journal of Geo-Information, 2024, 13(11): 378.
[11] Corso G, Stark H, Jegelka S, et al. Graph neural networks[J]. Nature Reviews Methods Primers, 2024, 4: 17.
[12] Scarselli F, Gori M, Tsoi A C, et al. The graph neural network model[J]. IEEE Transactions on Neural Networks, 2009, 20(1): 61-80.
[13] Kipf T N, Welling M. Semi-Supervised Classification with Graph Convolutional Networks[C]//International Conference on Learning Representations. 2017.
[14] Xu Y, Zhou B, Jin S, et al. A framework for urban land use classification by integrating the spatial context of points of interest and graph convolutional neural network method[J]. Computers, Environment and Urban Systems, 2022, 95: 101807.
[15] Xu R, Chen Z, Li F, et al. Identification of urban functional zones based on POI density and marginalized graph autoencoder[J]. ISPRS International Journal of Geo-Information, 2023, 12(8): 343.
[16] Veličković P, Cucurull G, Casanova A, et al. Graph Attention Networks[C]//International Conference on Learning Representations. 2018.
[17] He L, Bai L, Yang X, et al. High-order graph attention network[J]. Information Sciences, 2023, 630: 222-234.
[18] Vaswani A, Shazeer N, Parmar N, et al. Attention Is All You Need[C]//Advances in Neural Information Processing Systems. 2017, 30: 5998-6008.
[19] Huang C, Zhou Y, Wu T, et al. A cellular automata model coupled with partitioning CNN-LSTM and PLUS models for urban land change simulation[J]. Journal of Environmental Management, 2024, 351: 119828.
[20] Zhao X, Wang P, Gao S, et al. Combining LSTM and PLUS models to predict future urban land use and land cover change: A case in Dongying City, China[J]. Remote Sensing, 2023, 15(9): 2370.
[21] Yu B, Yin H, Zhu Z. Spatio-Temporal Graph Convolutional Networks: A deep learning framework for traffic forecasting[C]//Proceedings of the Twenty-Seventh International Joint Conference on Artificial Intelligence. 2018: 3634-3640.
[22] Guo S, Lin Y, Feng N, et al. Attention based spatial-temporal graph convolutional networks for traffic flow forecasting[C]//Proceedings of the AAAI Conference on Artificial Intelligence. 2019, 33(1): 922-929.
[23] Tan X, Chen W, Cao H, et al. Identifying spatiotemporal characteristics and driving factors of industrial land use morphology in China[J]. Expert Systems with Applications, 2024, 235: 121231.
[24] Lu W, Tao C, Ji Q, et al. Social information fused urban functional zones classification network[C]//ISPRS Annals of the Photogrammetry, Remote Sensing and Spatial Information Sciences. 2020, V-3-2020: 263-268.
[25] Tao Y, Liu W, Chen J, et al. A graph-based multimodal data fusion framework for identifying urban functional zone[J]. International Journal of Applied Earth Observation and Geoinformation, 2025, 136: 104353.
[26] Li C, Gao X, He B J, et al. Coupling coordination relationships between urban-industrial land use efficiency and accessibility of highway networks: Evidence from Beijing-Tianjin-Hebei urban agglomeration, China[J]. Sustainability, 2019, 11(5): 1446.
[27] Xie Y, Zhang Y, Gong M, et al. Mgat: Multi-view graph attention networks[J]. Neural Networks, 2020, 132: 180-189.
[28] Zhao A, Huang J, Gao F, et al. Regional allocation of industrial land in industrializing China: Does spatial mismatch exist?[J]. Landscape Research, 2023, 48(3): 396-411.
[29] Zhao X, Zhang L, Huang X, et al. Evolution of the spatiotemporal pattern of urban industrial land use efficiency in China[J]. Sustainability, 2018, 10(7): 2174.
[30] Oono K, Suzuki T. Graph Neural Networks Exponentially Lose Expressive Power for Node Classification[C]//International Conference on Learning Representations. 2020.
[31] He Q, Tang X. Identification and analysis of industrial land in China based on the point of interest data and random forest model[J]. Frontiers in Environmental Science, 2022, 10: 907383.